Research Square

Preprints are preliminary reports that have not undergone peer review.
They should not be considered conclusive, used to inform clinical practice,
or referenced by the media as validated information.

A C++/Fortran implementation of 3D cylindrical dust dynamics with Adams-Moulton integration: Application to TW Hydrae.

Loidel Puentes-Milián

loidelpuentes6@gmail.com

Instituto Superior de Tecnologías y Ciencias Aplicadas

Research Article

Keywords: protoplanetary disk, planetesimal formation, dust dynamics

Posted Date: November 20th, 2026

DOI: https://doi.org/10.21203/rs.3.rs-11601009/v1

License: This work is licensed under a Creative Commons Attribution 4.0 International License.
Read Full License

Additional Declarations: No competing interests reported.

A C++/Fortran implementation of 3D cylindrical dust dynamics with Adams-Moulton integration: Application to TW Hydrae.

Loidel Puentes-Milián[1]

[1]Department of Nuclear Physics, Instituto Superior de Tecnologías y Ciencias Aplicadas (InSTEC), University of Havana, Ave. Salvador Allende 1110, Plaza de la Revolución, 10400, Havana, Cuba.

Contributing authors: loidelpuentes6@gmail.com, loidel@instec.cu;

Abstract

The settling of grains of varying sizes has been studied under the conditions of the protoplanetary disk of TW Hydrae. By analyzing the temporal evolution of grain coordinates and velocities, the average settling time, radial drift times, and tilt angles were estimated. Similarly, the mean, maximum, and minimum Stokes number values were obtained, along with the dust vertical scale. Simulations were performed for 5 different grain radii, allowing for conclusions to be drawn about how grain size influences planetesimal formation.

Keywords: protoplanetary disk; planetesimal formation; dust dynamics.

1 Introduction

The vertical settling of particles in protoplanetary disks results from the competition between stellar gravity, which attracts the particles toward the midplane, and the aerodynamic drag exerted by the gas, which tends to pull them along with the flow. For spherical particles in the linear drag regime, the dynamics can be described by a system of 6 coupled differential equations. Calculations determine whether the particles mix due to turbulence, settle slowly as gas tracers, or undergo damped oscillations; furthermore, radial drift induced by the pressure gradient modifies the local residence and, therefore, the conditions that control settling [1–3].

Since settling efficiency depends strongly on the size and density of the gas, the presence of radial structures (rings, voids, pressure traps) alters the vertical distribution of dust and favors the accumulation of specific sizes in particular regions [4, 5]. Aerodynamic coupling between dust grains and gas in protoplanetary disks is a fundamental process that governs dust evolution, planetesimal formation, and ultimately, the architecture of planetary systems [6–10]. In particular, the braking time in the Epstein regime quantifies how quickly a dust grain adjusts its velocity to that of the surrounding gas due to aerodynamic drag. This parameter, along with the Stokes number, determines the dynamics of solids, their settling, radial migration, and the efficiency of mechanisms such as drag instability and dust trap formation.

The TW Hydrae (TW Hya) system is the prototype of a T Tauri-type protoplanetary disk, extensively studied due to its proximity (60 *pc*), near-face-on orientation, and abundance of ring substructures. It constitutes one of the most studied laboratories for understanding the evolution of dust and gas in young systems [11–22]. High-resolution observations with ALMA have revealed a complex ring-and-gap structure [15, 16, 20, 22], where the grain size distribution varies significantly with radius. Millimeter-sized particles or larger have been detected in the inner regions and bright rings [16, 19], while much smaller grains predominate in the outer regions [17, 18]. These results suggest a strong radial size gradient, associated with dust traps and filtering processes by forming planets.

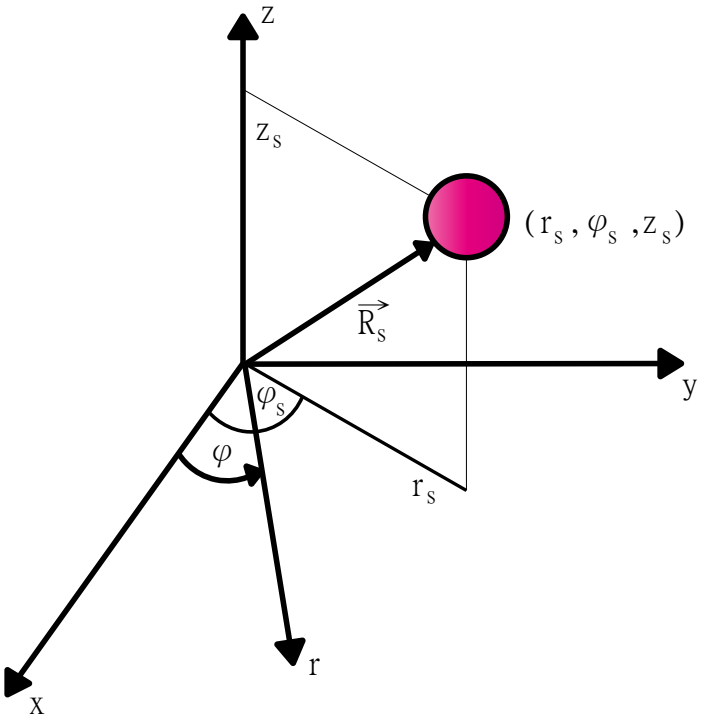


Fig. 1 Schematic representation of the coordinates chosen to describe the position of the grains.

In this context, it is essential to study the vertical settling of grains in three dimensions and in cylindrical coordinates (see Figure 1)), since aerodynamic coupling depends critically on particle size. For this work, five representative grain radius values were chosen: $a = 1, 5, 10, 50, 100\ mm$. These range from particles well coupled to the gas to bodies with sufficient inertia to experience faster settling and significant radial drift. The objective of this study is to characterize how grain size influences vertical evolution in the TW Hydrae disk, integrating numerical calculations in 3D cylindrical coordinates with the observational constraints reported in the literature.

In this work, average settling times, vertical dust scales, radial drift times, maximum, minimum, and average Stokes number values, and tilt angles were quantified. The results allowed for a discussion of the implications of the a value for coagulation and planetesimal formation in regions where millimeter-sized and larger grains are detected.

The structure of this article is as follows: Section 1 consists of this introduction; Section 2 is dedicated to explaining the methodology used for the simulation, as well as the one followed to generate the initial conditions, along with the details of the numerical calculation; Section 3 shows the results of the simulation accompanied by their respective discussion; and Section 4 states the conclusions of the work.

2 Methodology

The methodology used in this work is based on obtaining the system of differential equations that describe the evolution of dust grains in protoplanetary disks. For this, it is necessary to consider that the kinetic energy of the grains is equal to:

$$T = \frac{1}{2} m \left(v_r^2 + v_\varphi^2 + v_z^2 \right) \tag{1}$$

where v_r, v_φ and v_z are the components of the grain velocity and m is the mass of the grain, which, in the case of spherical grains, is calculated as:

$$m = \frac{4}{3} \pi a^3 \rho_s \tag{2}$$

where ρ_s is the material density of the grain. The value adopted in this work is 3 g/cm^3, taken from Ref. [19].

The potential energy of the grains is equal to:

$$U = -\frac{GMm}{\sqrt{r^2 + z^2}} \tag{3}$$

where G is the universal gravitational constant, equal to $6.674 \cdot 10^{-8}\ cm^3/g \cdot s^2$, and M is the mass of the star, with a value equal to 0.8 times the mass of the Sun [13, 17, 19].

It is now taken into account that, for a conservative system, the equations of motion can be derived from the Hamiltonian of said system (H), which is equal to the sum

of its kinetic and potential energies, through the following relationships:

$$\frac{dq_i}{dt} = \frac{\partial H}{\partial p_i} \tag{4}$$

$$\frac{dp_i}{dt} = -\frac{\partial H}{\partial q_i} \tag{5}$$

where q_i and p_i represent the generalized coordinates and moments respectively.

However, in the case of interest, there are dissipative forces, which are non-conservative forces and cannot be obtained from a simple Hamiltonian. In the presence of gas-grain drag, radiation, or friction, force terms are added to the moment equations:

$$\frac{dp_i}{dt} = -\frac{\partial H}{\partial q_i} + F_i^{NC} \tag{6}$$

where the superscript NC refers to non-conservative forces. In the specific case of gas-grain drag, as is the case here, the force term has the form [2]:

$$\vec{F}_{arras} = -\frac{m}{t_s}\vec{v}_{rel} \tag{7}$$

where t_s is the stopping time (see Subsection 2.1) and r_rel is the gas-grain relative velocity (see Subsection 2.2). If the drag is linear, the relative velocity is equal to:

$$\vec{v}_{rel} = \vec{v}_{grain} - \vec{v}_{gas} \tag{8}$$

Thus, the system of 6 coupled differential equations used in this work is as follows:

$$\frac{dr}{dt} = v_r \tag{9}$$

$$\frac{d\varphi}{dt} = \frac{v_\varphi}{r} \tag{10}$$

$$\frac{dz}{dt} = v_z \tag{11}$$

$$\frac{dv_r}{dt} = \frac{v_\varphi^2}{r} - \frac{GMr}{(r^2+z^2)^{3/2}} - \frac{v_r - v_{r\,gas}(r,z)}{t_s(r,z)} \tag{12}$$

$$\frac{dv_\varphi}{dt} = -\frac{v_r v_\varphi}{r} - \frac{v_\varphi - v_{\varphi\,gas}(r,z)}{t_s(r,z)} \tag{13}$$

$$\frac{dv_z}{dt} = -\frac{GMz}{(r^2+z^2)^{3/2}} - \frac{v_z - v_{z\,gas}(r,z)}{t_s(r,z)} \tag{14}$$

The term $v_r v_\varphi / r$, which appears in the equation for v_φ, arises because the radial movement of the grain changes the arm r of the angular motion and because the directions rotate. It is a geometric term, not an additional force, as it only reflects the coupling between radial and angular motion, like a Coriolis effect in non-Cartesian coordinates.

2.1 Stopping time

The stopping time quantifies how quickly a dust grain adjusts its speed to that of the surrounding gas due to aerodynamic drag. This parameter determines the dynamics of solids, their sedimentation, radial migration, and the efficiency of mechanisms such as drag instability and dust trap formation.

The expression used for stopping time depends on the current flow regime. The Epstein drag regime is applicable when the grain size is less than the mean free length (λ) of the gas, specifically, when:

$$a < \frac{9}{4}\lambda \tag{15}$$

This condition is met in the region considered for grains of the sizes taken into account. In this regime, the stopping time is expressed as [1, 5, 19]:

$$t_s(r,z) = \frac{\rho_s a}{\rho_g(r,z) v_{th}(r,z)} \tag{16}$$

where $\rho_g(r,z)$ is the density of the gas, and is expressed as [12, 17, 23, 24]:

$$\rho_g(r,z) = \rho_g(r,0) e^{-\frac{z^2}{2H^2(r,0)}} \tag{17}$$

where $\rho_g(r,0)$ is the gas density in the midplane, and is expressed as [23]:

$$\rho_g(r,0) = \frac{\Sigma_g(r)}{\sqrt{2\pi} H(r,0)} \tag{18}$$

where here $\Sigma_g(r)$ is the surface density of the gas, which is fitted with an exponentially truncated power law [13, 17, 19]:

$$\Sigma_g(r) = \Sigma_c \left(\frac{r}{r_c}\right)^{-\gamma} e^{-\left(\frac{r}{r_c}\right)^{2-\gamma}} \tag{19}$$

The chosen values for the parameters shown in Equation 19 are $\Sigma_c = 30\ g/cm^2$, $r_c = 35\ AU$ and $\gamma = 1.0$ [13, 19].

The function $H(r,z)$ shown in Equation 18 is called the height scale and is defined as [13, 20, 23]:

$$H(r,z) = \frac{c_s(r,z)}{\Omega_K(r,z)} \tag{20}$$

where $c_s(r,z)$ is the speed of sound, whose expression is the following [4, 16]:

$$c_s(r,z) = \sqrt{\frac{k_B T(r,z)}{\mu m_p}} \tag{21}$$

where $k_B = 1.3806{\cdot}10^{-16}\ erg/K$ is the Boltzmann constant, $m_p = 1.6735{\cdot}10^{-24}\ g$ is the mass of hydrogen, and μ is the average molecular weight. The value used in this

work for μ was 2.37 [20]. $T(r,z)$ refers to the temperature, whose expression is the following [20]:

$$T(r,z) = \begin{cases} T_{atm}(r) + [T_{mid}(r) - T_{atm}(r)] \cos^4\left[\frac{\pi z}{2 z_q(r)}\right] & z < z_q(r) \\ T_{atm}(r) & z \geq z_q(r) \end{cases} \tag{22}$$

where $T_{mid}(r)$ and $T_{atm}(r)$ are the temperatures of the midplane and the atmosphere respectively, and are defined as [20, 21]:

$$T_{mid}(r) = T_{0\,mid} \left(\frac{r}{r_0}\right)^{-q} \tag{23}$$

$$T_{atm}(r) = T_{0\,atm} \left(\frac{r}{r_0}\right)^{-q} \tag{24}$$

where the parameter values were taken from Ref. [20] and are as follows: $T_{0\,mid} = 40$ K, $T_{0\,atm} = 125$ K, $r_0 = 10$ AU and $q = 0.47$.

On the other hand, $z_q(r)$ is the so-called transition height, and its form is:

$$z_q(r) = \chi H(r,0) \tag{25}$$

having taken in this work $\chi = 4$ [13, 20].

In Equation 20, the Keplerian angular frequency is also used, represented by $\Omega_K(r)$ and which has the form [1, 3, 12, 16, 23]:

$$\Omega_K(r,z) = \sqrt{\frac{GM}{(r^2+z^2)^{3/2}}} \tag{26}$$

The function $v_{th}(r,z)$ used in Equation 16 is the average thermal speed of the gas molecules, whose relationship to the speed of sound is as follows [23, 24]:

$$v_{th}(r,z) = \sqrt{\frac{8}{\pi}} c_s(r,z) \tag{27}$$

2.2 Subkeplerian gas velocity components

A key aspect of circumstellar disk dynamics is the deviation of the gas from pure Keplerian motion, a phenomenon known as sub-Keplerian rotation, which arises due to pressure support and other physical effects present in the disk. In this context, the gas in protoplanetary disks does not orbit at exactly the Keplerian speed, but rather at a slightly lower speed, primarily due to the radial pressure gradient that acts as an additional centrifugal force. This difference, although small (on the order of 1 % to 5 %), has profound consequences for dust dynamics, solid migration, and planetesimal formation. The headwind experienced by solid particles induces rapid radial drift, which can be mitigated by pressure traps (rings and vortices) or by the formation of

planets that sculpt the disk. Furthermore, vertical velocity stratification can favor the concentration of solids in certain layers, facilitating the formation of planetary cores. The accurate characterization of the three velocity components is therefore essential to model the evolution of the disk and predict the final architecture of the planetary system.

The radial component reflects the transport of mass towards the center of the disk, driven by turbulent viscosity, and is therefore negative; moreover, it decreases with radius. These flows are responsible for the secular evolution of the disk and the feeding of the central star. Being dominated by viscous accretion, it is described by the Shakura-Sunyaev disk theory [25–27]:

$$v_{r\,gas}(r,z) = -\frac{3}{\Sigma(r) r^{1/2}} \frac{\partial}{\partial r} \left[\nu(r,z) \Sigma(r) r^{1/2} \right] \tag{28}$$

where:

$$\nu(r,z) = \frac{\alpha c_s^2(r,z)}{\Omega_K(r,z)} \tag{29}$$

is the kinematic viscosity [4, 18, 19], where α is the turbulent viscosity parameter. In this work, the value reported in Ref. [18] ($\alpha = 10^{-2}$) was used.

The azimuthal component is dominant in gas kinematics. The difference between the actual gas velocity and the pure Keplerian velocity is a direct manifestation of pressure support. This difference is crucial for solid migration and planetesimal formation, as it induces rapid radial drift of particles 1 m in size, a phenomenon known as the meter barrier. Furthermore, local perturbations (spiral waves, planet-disk interaction) They can induce additional variations in $v_{\varphi\,gas}(r,z)$, detectable as spiral patterns on velocity maps. This velocity, considering the pressure support, is expressed as [5]:

$$v_{\varphi\,gas}(r,z) = v_K(r,z)\sqrt{1-\eta(r,z)} \tag{30}$$

where $v_K(r,z)$ is the Keplerian velocity, defined as [5, 12]:

$$v_K(r,z) = \sqrt{\frac{GM}{\sqrt{r^2+z^2}}} \tag{31}$$

and $\eta(r,z)$ is the parameter that measures the deviation of the gas from the Keplerian velocity, and is calculated as [23, 28]:

$$\eta(r,z) = -\frac{1}{2}\left[\frac{c_s(r,z)}{v_K(r,z)}\right]^2 \frac{\partial \ln P(r,z)}{\partial \ln r} \tag{32}$$

where:

$$P(r,z) = \rho_g(r,z) c_s^2(rz) \tag{33}$$

It's the gas pressure.

The z-component of the gas velocity is related to hydrostatics, meridional flows, and local disturbances. In the midplane, the gas is in vertical hydrostatic equilibrium,

so $v_z \approx 0$. Outside of this plane, meridional flows and local disturbances (spiral waves, winds, etc.) induce vertical velocities. The expression to obtain it is:

$$v_{z\,gas}(r,z) = C_{mer}\frac{\nu(r,z)}{r}\frac{z}{H(r,z)} \tag{34}$$

where C_{mer} is a dimensionless factor that adjusts the intensity of the meridional flow. The value chosen in this work was 10^{-1}.

2.3 Initial conditions

This section began by stating that, in order to study the dynamics of grains, one must solve the Cauchy problem for a system of 6 coupled differential equations (9–14). The first step in solving this task is to determine, for each trajectory, the 6 values that define the initial phase point $\tau^0 = (r^0, \varphi^0, z^0, v_r^0, v_\varphi^0, v_z^0)$ [29].

To generate the values of r_i^0, the surface density of the gas was sampled (see Equation 19), since it was assumed that the dust and gas were initially mixed. Thus, the probability of placing a particle in a ring between r and $r + dr$ is proportional to $\Sigma(r)2\pi r dr$. Since $\Sigma(r)$ is largely proportional to $r^{-\gamma}$, this results in a radial density function that can be sampled by inversion. Therefore, the cumulative inverse function is equal to:

$$F(r) = \frac{r^p - r_{in}^p}{r_{out}^p - r_{in}^p} \tag{35}$$

where r_{in} and r_{out} are the inner and outer radii of the disk, respectively. In this work, the values $r_{in} = 4\ AU$ and $r_{out} = 215\ AU$ from Refs. [13, 19] were used. Since the value used in this work for γ was 1.0, the values of r_i^0 were generated from the following expression:

$$r_i^0 = r_{in} + U(0,1)(r_{out} - r_{in}) \tag{36}$$

where $U(0,1)$ is a function that generates random values between 0 and 1. This is equivalent to saying that random values between 4 AU and 215 AU were generated.

There are no restrictions for the azimuthal coordinate (no asymmetries), so random values of φ_i^0 were generated in the interval $[0, 2\pi)$.

To generate the z_i^0 values, samples were taken from a Gaussian distribution with mean 0 and standard deviation $H(r,0)$. That is:

$$z_i^0 = \mathcal{N}[0, H^2(r,0)] \tag{37}$$

This allowed for the generation of well-mixed initial conditions. However, the sampling was truncated at $\pm\ 3H(r,0)$ to avoid particles in extreme tails that are not physically realistic in the model used.

To generate the initial values of the velocity components, the values they take for the stationary case $\vec{v} = \vec{0}$ were first obtained, and then random components were added to model turbulence.

For the radial component, the expression derived from the stationary case is [28]:

$$v_{r_0} = \frac{v_{r\,gas}(r,z) + 2St(r,z)[v_{\varphi\,gas}(r,z) - v_K(r,z)]}{1 + St^2(r,z)} \tag{38}$$

where $St(r,z)$ is the Stokes number, which is defined as [5, 23, 24]:

$$St(r,z) = t_s(r,z)\Omega(r,z) \tag{39}$$

Therefore, the values of $v^0_{r_i}$ were generated from the expression:

$$v^0_{r_i} = v_{r_0} + \mathcal{N}[0, \sigma^2_{v_r}] \tag{40}$$

being:

$$\sigma_{v_r} = f_{turb}\sqrt{\alpha}c_s(r,z) \tag{41}$$

where f_{turb} is a parameter used to adjust how much noise is introduced. The value used was 1.0.

On the other hand, for the azimuthal component the expression derived from the stationary case is [28]:

$$v_{\varphi_0} = v_{\varphi\,gas}(r,z) + \frac{-St(r,z)v_{r\,gas}(r,z) + [v_{\varphi\,gas}(r,z) - v_K(r,z)]}{1 + St^2(r,z)} \tag{42}$$

Therefore, the values of $v^0_{\varphi_i}$ were generated from the expression:

$$v^0_{\varphi_i} = v_{\varphi_0} + \mathcal{N}[0, \sigma^2_{v_\varphi}] \tag{43}$$

where:

$$\sigma_{v_\varphi} = \sigma_{v_r} \tag{44}$$

Finally, for the vertical component, the expression derived from the stationary case is [28]:

$$v_{z_0} = v_{z\,gas}(r,z) - t_s(r,z)\frac{GMz}{(r^2+z^2)^{3/2}} \tag{45}$$

Generating the values of $v^0_{z_i}$ from the equation:

$$v^0_{z_i} = v_{z_0} + \mathcal{N}[0, \sigma^2_{v_z}] \tag{46}$$

where it was taken:

$$\sigma_{v_z} = \sigma_{v_\varphi} = \sigma_{v_r} \tag{47}$$

2.4 Numerical calculation details

Under the conditions mentioned in the previous subsection, $5 \cdot 10^3$ sets of initial conditions were generated. It is known from accumulated experience in studies involving simulation [30–36], that this quantity is sufficient to make the results converge.

For the numerical integration of the system of equations (4−9), an Adams-Moulton algorithm of 4^{th} order was used, which is a predictor-corrector method that has the drawback of not being self-initializing. To initialize it, we used a Runge-Kutta integrator, also of 4^{th} order.

Each of the $5 \cdot 10^3$ trajectories was propagated as long as the following condition was met:

1. The radial derivative of the non-positive pressure, that is:

$$\frac{\partial P(r,z)}{\partial r} \leq 0 \tag{48}$$

   Otherwise, the grain tends to move away from the mid-plane of the disk and never settles.
2. The propagation time did not exceed a certain $t_{max} = 3 \cdot 10^6\ years$.
3. The grain was not considered settled.

The grains were considered settled once 3 conditions were met simultaneously:

1. Absolute vertical position:

$$|z| \leq \epsilon_z H_p(r) \tag{49}$$

   where $\epsilon_z = 10^{-1}$ and:

$$H_p(r) = H(r,0)\sqrt{\frac{\alpha}{\alpha + St(r,0)}} \tag{50}$$

2. Low vertical speed:

$$|v_z| \leq \epsilon_v c_s(r,0)\sqrt{\frac{\alpha}{\alpha + St(r,0)}} \tag{51}$$

   where $\epsilon_v = 10^{-1}$.
3. Vertical energy decay:

$$\frac{v_z^2}{2} \leq \epsilon_E \frac{c_s^2(r,0)\alpha}{2[\alpha + St(r,0)]} \tag{52}$$

   where $\epsilon_E = 10^{-2}$.

The time step used throughout the simulation was variable; it was taken to be 4 orders of magnitude smaller than the smallest value between $t_s(r,z)$ and $\Omega_K^{-1}(r,z)$, that is:

$$\Delta t = 10^{-4} \cdot min\left[t_s(r,z), \frac{1}{\Omega_K(r,z)}\right] \tag{53}$$

C++ and Fortran were used as programming languages.

3 Results and discussion

3.1 Average settling times

The settling time is the characteristic time it takes for a particle to lose height and approach the middle layer of the disk due to the action of vertical gravity and the drag of the gas.

To calculate the average settling time, an exponential decay law is used, such as that followed by radioactive decay [38–41]. For an amount N that decreases exponentially according to the formula:

$$N(t) = N_0 e^{-\lambda t} \tag{54}$$

where N_0 is the initial quantity, the average lifetime is defined as:

$$\tau = \frac{1}{\lambda} \tag{55}$$

In this case, the quantity N was the number of trajectories for which the grains had not settled. Despite this, non-exponential behavior sometimes appears in the decays for short times.

For adjusting the simulation results, 2 types of adjustments were used: one and two exponentials adjustments.

$$\frac{N_{\mathrm{NS}}(t)}{N_{\mathrm{T}}} \sim \alpha_1 e^{-\alpha_2 t} \tag{56}$$

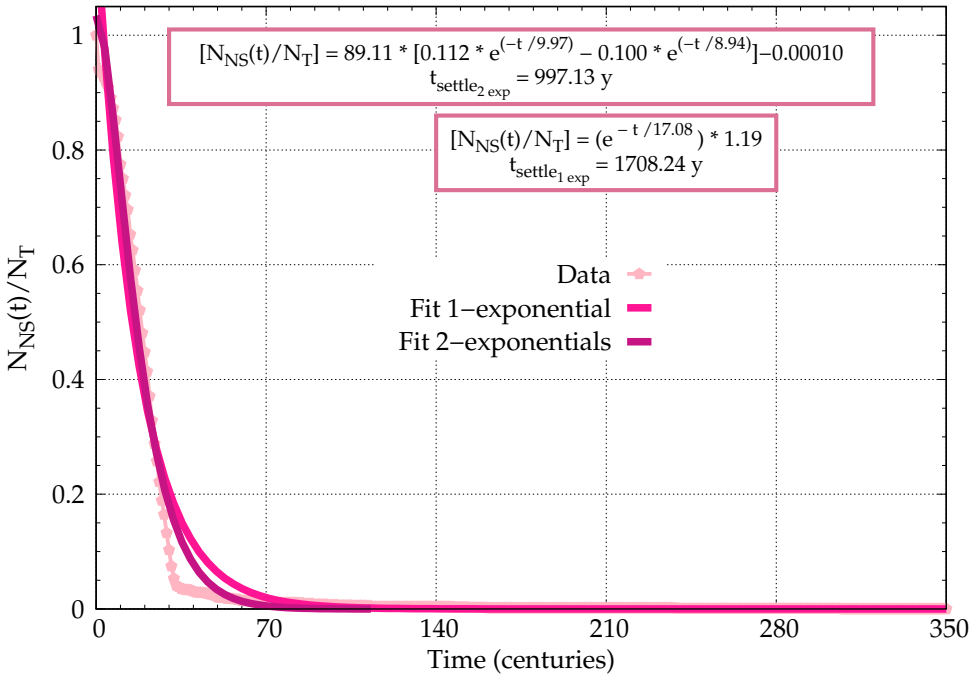


Fig. 2 1 and 2 exponential fits for $a = 1\ mm$. The boxes within the graph show the equations used in the fit along with the average settling times.

Table 1 Average settling times (y) of the powder grains. The first column corresponds to the grain size (mm) used in the simulation. The second and third columns correspond to the values obtained with the 1 and 2 exponential adjustments, respectively.

a	1 exp.	2 exp.
1	1708.24	997.13
5	586.56	300.95
10	472.93	222.64
50	990.04	461.26
100	1217.35	523.87

$$\frac{N_{\mathrm{NS}}(t)}{N_{\mathrm{T}}} \sim (\alpha_1 e^{-\alpha_2 t} - \alpha_2 e^{-\alpha_1 t}) \qquad \alpha_1 > \alpha_2 \tag{57}$$

where N_{NS} is the number of unsettled trajectories after time t, N_T is the total number of these for $t = 0$, and α_1 and α_2 are different adjustment parameters for each grain size.

The parameter α_1 is associated with the energy transfer mechanisms that move the particle away from the midplane. It has a significant influence only at the beginning, and its function is to allow for a better fit in the region near the plateau that appears for short times. The parameter α_2 is related to the average settling time through the following relationship:

$$t_{settle} = \frac{1}{\alpha_2} \tag{58}$$

The adjustments made to the results obtained for the radius $a = 1\ mm$ are shown in Figure 2. This figure shows the 2 equations that describe the behavior of the average settling time. Table 1 lists the average settling times given in years for each grain size.

Figure 3 presents the average settling times shown in Table 1. The results were plotted on a semi-radical scale; that is, the values on the x-axis are on a radical scale, and those on the y-axis are on a conventional linear scale. This was done to avoid the values appearing clustered, given that radii of different orders of magnitude were used. Furthermore, it can be seen that there is no general trend toward either an increase or decrease in settling times with increasing grain radius. This means that, although the longest average settling times were observed for the smallest grains, it cannot be said that, on average, larger grain size results in shorter settling times. The valley obtained for $a = 10\ mm$ indicates that, within the studied range, this value guarantees the fastest settling of the grains. All of this suggests that grains of this size must be more abundant than those outside the mid-plane, as they settle faster than the others. On the other hand, the smallest grains must be the most abundant, since their average settling time is long; the values obtained with both adjustments are close to a millennium. Another important conclusion is that the results obtained with the 2-exponential adjustment are always lower than those obtained with the 1-exponential adjustment, and this is because the latter do not always fit the data obtained for short times well.

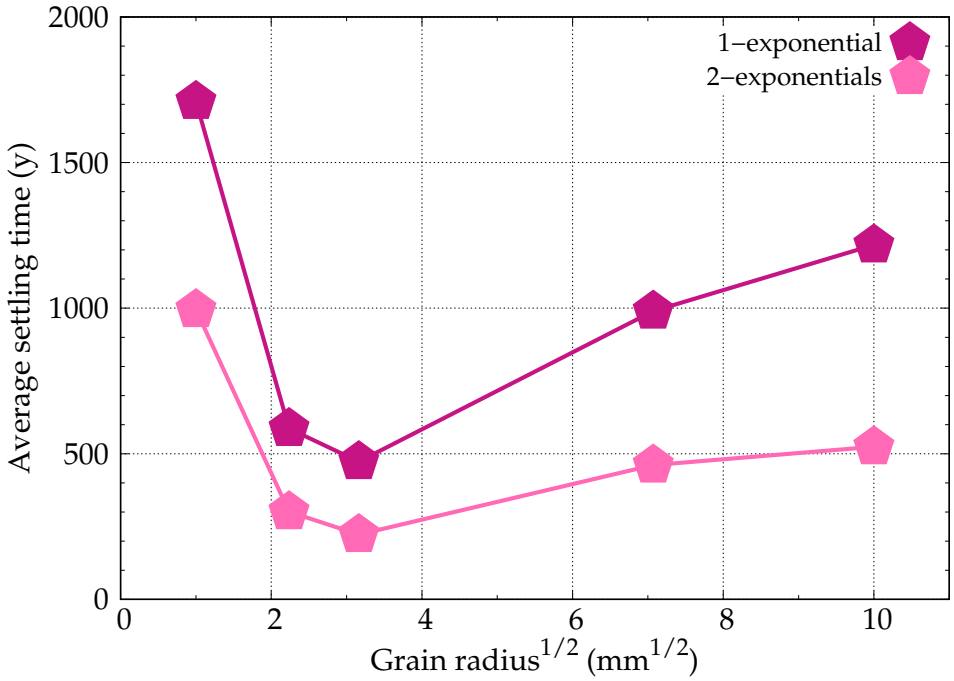


Fig. 3 Settling times obtained using exponential 1 and 2 adjustments. The x-axis shows the value that must be squared to obtain the grain radius. The lines connect the points that correspond to the same data type.

3.2 Radial drift time

The radial drift time is the characteristic time it takes for a dust particle to travel radially through the protoplanetary disk, usually inwards, due to its relative drift with respect to the gas. It is defined as [3]:

$$t_{drift} = \frac{r}{|v_r|} \tag{59}$$

To determine the distributions of the final values of the radial drift times, the *Standard Binning* method was used, whose expression is as follows:

$$P(r_1) = \frac{1}{N_S} \sum_{i=1}^{N_S} H\left[\frac{1}{2}(r_2 + r_1) - r_i\right] \cdot H\left[r_i - \frac{1}{2}(r_1 + r_0)\right] \tag{60}$$

where $P(t_1)$ represents the probability that the radial drift time value is t_1 once the grain has settled vertically, N_S is the number of settled paths, t_i is the radial drift time obtained after grain settling for path i, and $H(x)$ is the Heaviside step function, where $H(x) = 1$ when $x > 0$ and $H(x) = 0$ when $x < 0$. In this case, it has also been assumed that $H(x) = 1$ when $x = 0$. Essentially, this method rounds the values, that

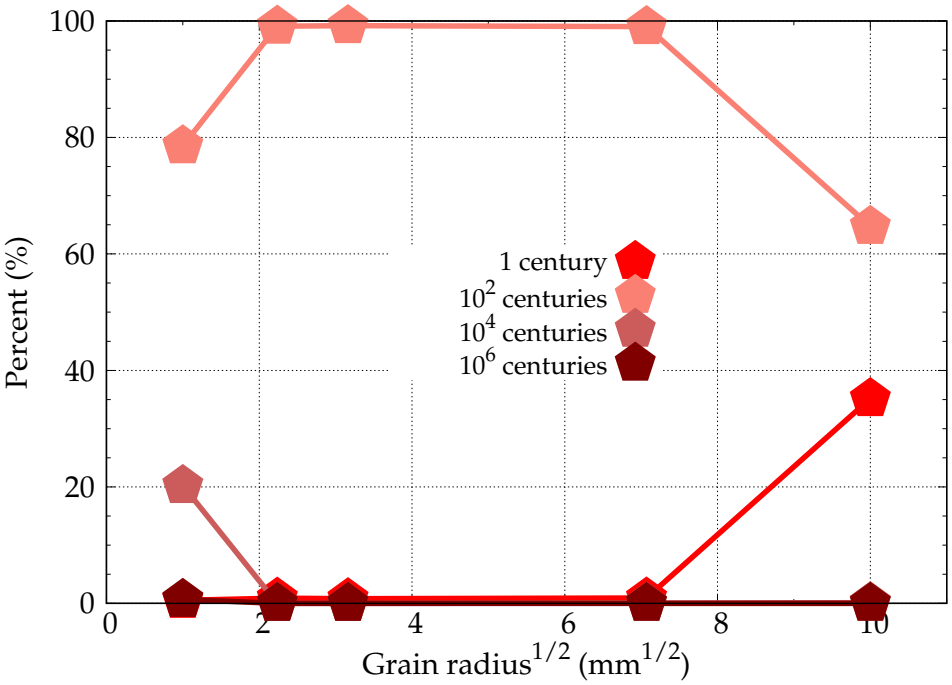


Fig. 4 Percentages obtained for the radial drift times chosen as a reference. The numbers shown within the graph correspond to the values at which the results were grouped. The x-axis shows the value that must be squared to obtain the grain radius. The lines connect the points that correspond to the same type of data.

is, it allows grouping the data based on certain values of interest. For this reason, this method is used to discretize quantities that are treated as if they were continuous.

Figure 4 shows, on a semi-radical scale, the distributions obtained for radial drift time, in centuries, when applying the Standard Binning method. It can be seen that larger grains drift radially faster after settling than other grains, as they have the highest percentages for the smallest drift times. The smallest ratio obtained (1 *century*) is only significant for the largest radius. Conversely, the highest ratio was obtained only for the smallest radius, but its percentage did not even exceed 1 %, meaning that, for grains of the considered size, the probability of the radial drift time being between 10^5 y 10^6 *centuries* is less than 1 %. It can also be seen that the dominant ratio for all grain sizes is 100 *centuries*.

3.3 Stokes Number

The Stokes number in studies of dust in protoplanetary disks is a dimensionless measure that indicates how strongly a particle is coupled to the gas.

Figure 5 shows the maximum, minimum, and average Stokes number for each grain size on a semiradical scale. It is evident that the maximum, minimum, and average values increase with increasing grain size, indicating that the coupling of the grains to the gas is closely dependent on their size. Thus, particles with a radius of 1 *mm* exhibit weak coupling to the gas, so their motion is almost like that of the gas in some

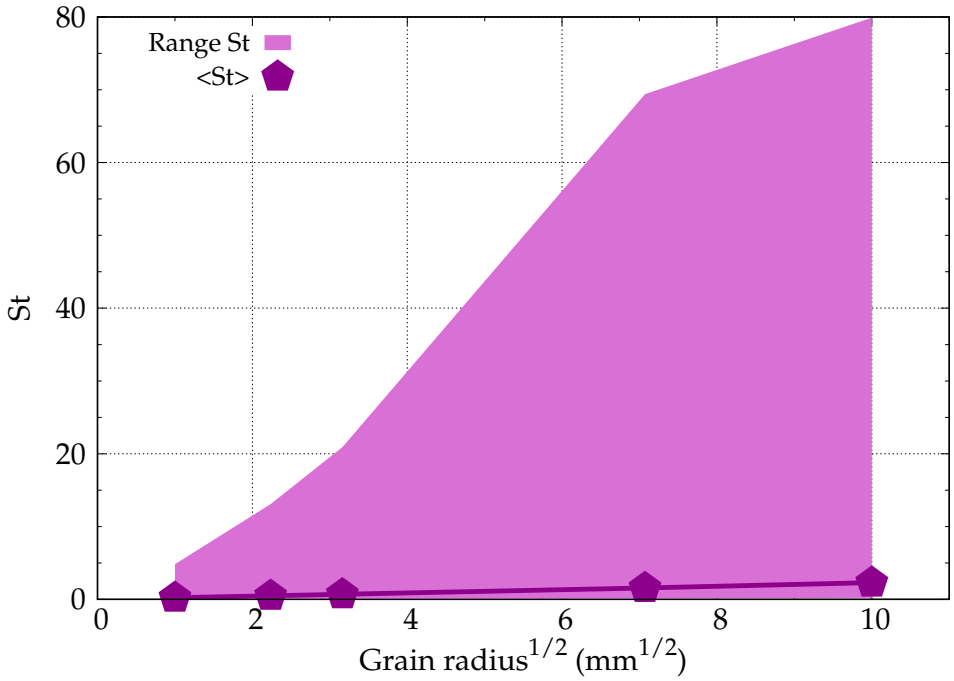


Fig. 5 Range of values alongside the average values obtained for the Stokes number, and for each grain size. The x-axis shows the value that must be squared to obtain the grain radius. The lines connect the points that correspond to the same data type.

cases. On the other hand, for particles of 5 and 10 mm, gravity and drag compete, causing these particles to drift radially faster toward the center of the disk. This latter finding is entirely consistent with the results shown in Figure 4. Finally, grains with $a = 50$ and 100 mm are weakly coupled to the gas; that is, they follow almost ballistic orbits and barely experience the gas.

3.4 Inclination

The inclination i is an orbital parameter that describes the angle between the plane of a particle's or body's orbit and a reference plane. In protoplanetary disks, the reference plane is usually the disk's midplane. Mathematically:

$$i = \arccos\left(\frac{h_z}{\vec{h}}\right) \tag{61}$$

where:

$$\vec{h} = \vec{r} \times \vec{v} \tag{62}$$

is the specific angular momentum vector of the dust grain.

Figure 6 illustrates the distributions of the tilt angles, in degrees, as fractional populations. These values were obtained at the end of the simulation, that is, once the grain had settled. The fraction of the total population refers to the fraction of

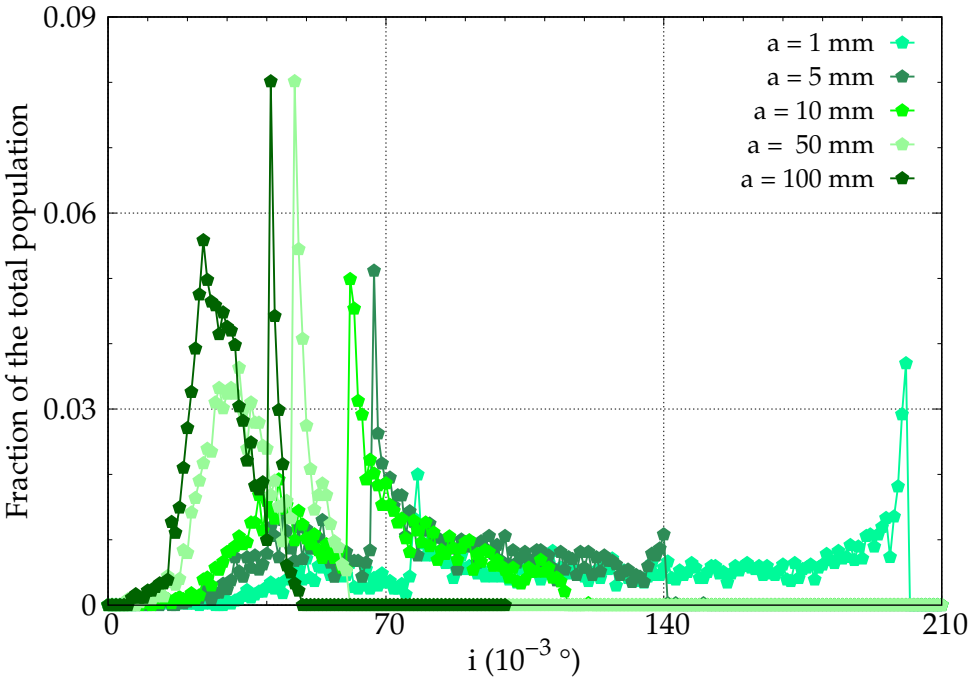


Fig. 6 Distribution of fractional populations corresponding to orbital inclination. The y-axis shows the fraction of the total population that each value represents. The x-axis shows the value that must be multiplied by 10^{-3} to obtain the inclination in degrees. The lines connect the points that correspond to the same data type.

trajectories that had the corresponding value of i. A fraction equal to 0.02, for a grain radius a corresponding to the tilt value i, means that 2 % of the trajectories that settled, out of the total $5 \cdot 10^3$ simulated for grain size a, had a final tilt equal to i. This 2 % represents the probability that , after settling, the tilt of the orbit of the grain of size a will reach the value i. These distributions are calculated by taking all the values of the final tilts and then counting how many times each value is repeated, to finally calculate the fraction of the population. If the inclination $i = i_1$ was obtained after $3 \cdot 10^3$ of $5 \cdot 10^3$ settled configurations, then the fraction of i_1 will be $3 \cdot 10^3 / 5 \cdot 10^3 = 0.6$. As can be seen, small inclinations, very close to 0, were obtained for all sizes. This means that all orbits are quasi-planar, that is, they are not perfectly coplanar since they have a small inclination. The figure shows that the larger particles have orbits that are closer to coplanar, while the smaller ones oscillate slightly above and below the midplane.

3.5 Vertical scale of dust

The vertical scale of dust (H_d) in a protoplanetary disk is a measure of how coarse or flattened the dust grain distribution is relative to the disk's midplane. It is analogous to the height scale of gas, but modified by the balance between particle turbulence and settling.

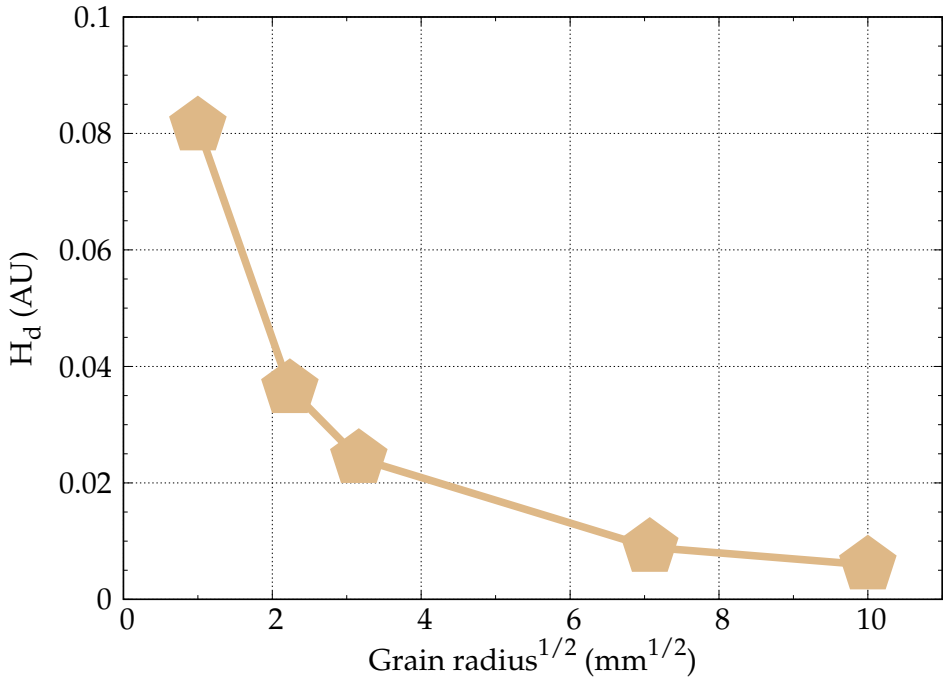


Fig. 7 Vertical scale of the powder obtained for each grain size. The x-axis shows the value that must be squared to obtain the grain radius. The lines connect the points that correspond to the same data type.

If the particles have coordinates z_i with respect to the midplane [24]:

$$H_d = \sqrt{\frac{1}{N}\sum_{i=1}^{N}(z_i - \bar{z})^2} \tag{63}$$

where N is the total number of settled particles.

Figure 7 shows the vertical scale value of the powder for each grain size, given in AU, also on a semi-radical scale. It can be seen that the thickness of the powder layer decreases in a manner similar to exponential decay, with increasing grain size. This result may seem peculiar considering that larger particles naturally occupy more space; that is, if we imagine an ideal case where the particles accumulate perfectly vertically on top of each other, 100 particles with a radius of 1 mm would be needed to achieve the same height as one particle with a radius of 100 mm. However, this is not the case, as the inclination must be taken into account. This is because particles with a small inclination concentrate near the midplane, while those with greater inclinations contribute to thickening the powder layer. As seen in Figure 6, the smaller the particle, the greater its inclination, and therefore the greater the thickness of the powder layer, and vice versa. This result summarizes what is observed in Figure 7 without exception.

4 Conclusions

The settling of dust grains has been studied under the conditions of the protoplanetary disk of the TW Hydrae system. Average settling times were estimated, and the shortest times were obtained for grains with radii of 5 and 10 mm. Obtaining the distributions for radial drift times showed that the grains that migrate radially most easily are those with these same sizes; therefore, outside the interior of the disk's midplane, grains on the order of centimeters in size should not be abundant. The Stokes number confirmed these results, as grains with a value closest to unity migrate radially the fastest; it also showed that large particles are not coupled to the gas, unlike small ones. Similarly, by obtaining the inclination of the orbits, it was observed that the smaller grains have less coplanar trajectories than the rest, although all inclination values turned out to be small. These results were perfectly compatible with those obtained when calculating the thickness of the powder layer, since it was greater as the grain became smaller, due to the inclination of its orbit.

Declarations

Ethics approval and consent to participate

Not Applicable

Availability of data and materials

The data that support the findings of this study are available from the corresponding author upon reasonable request.

Competing interests

The author declare that they have no known competing financial interests or personal relationships that could have appeared to influence the work reported in this paper.

Funding

Not Applicable

Authors? contributions

Loidel Puentes-Mili?n: Writing - review & editing, Writing - original draft preparation, Visualization, Validation, Software, Methodology, Investigation, Formal analysis, Data curation, Conceptualization, Supervision, Resources.

Acknowledgements

The author acknowledge the support from PN223LH010-060 project from InSTEC-UH. The author would also like to thank Adriana Monteagudo-Rivero, the editor and the anonymous referee for their comments that helped improve the manuscript.

Authors' information

ORCID

Loidel Puentes-Milián - https://orcid.org/0009-0009-4226-4198

References

[1] S. J. Weidenschilling, *Mon. Not. R. Astr. Soc.* **180**, *57* (1977).

[2] G. Laibe, D. J. Price, *Mon. Not. R. Astr. Soc.* **420**, *2345* (2012).

[3] I. Adachi, C. Hayashi, K. Nakazawa, *Prog. Theo. Phys.* **56**, *1756* (1976).

[4] M. Li, S. Huang, Z. Zhu, M. I. Petaev, J. H. Steffen, *MNRAS* **503**, *5254* (2021).

[5] R. Alexander, *Lecture 3: Dust dynamics and planetesimal formation.*

[6] E. Kokubo, S. Ida, *Astro. J.* **581**, *666* (2002).

[7] X. Sun, S. Zheng, Z. Shi, B. Liu, R. Yang, *Universe* **10**, *310* (2024).

[8] L. Cesario, T. Lichtenberg, E. Alei, Ó. Carrión-González, F. A. Dannert, D. Defrère, S. Ertel, A. Fortier, A. García-Muñoz, A. M. Glauser, J. T. Hansen, R. Helled, P. A. Huber, M. J. Ireland, J. Kammerer, R. Laugier, J. Lillo-Box, F. Menti, M. R. Meyer, L. Noack, S. P. Quanz, A. Quirrenbach, S. Rugheimer, F. van der Tak, H. S. Wang, M. Anger, O. Balsalobre-Ruza, S. Bhattarai, M. Braam, A. Castro-González, C. S. Cockell, T. Constantinou, G. Cugno, J. Davoult, M. Güdel, N. Hernitschek, S. Hinkley, S. Itoh, M. Janson, A. Johansen, H. R. A. Jones, S. R. Kane, T. A. van Kempen, K. G. Kislyakova, J. Korth, A. B. Kovačević, S. Kraus, R. Kuiper, J. Mathew, T. Matsuo, Y. Miguel, M. Min, R. Navarro, R. M. Ramirez, H. Rauer, B. V. Ricketti, A. Romagnolo, M. Schlecker, E. L. Sneed, V. Squicciarini, K. G. Stassun, M. Tamura, D. Viudez-Moreiras, R. D. Wordsworth, *A&A* **692**, *A172* (2024).

[9] R. K. Mann, S. M. Andrews, J. A. Eisner, J. P. Williams, M. R. Meyer, J. Di Francesco, J. M. Carpenter, D. Johnstone, *Astro. J.* **802**, *77* (2015).

[10] K. Kornet, T. F. Stepinski, M. R'ożyczka, *A&A* **378**, *180* (2001).

[11] K. R. Schwarz, R. Teague, E. A. Bergin, *Astro. J. Lett.* **876**, *L13* (2019).

[12] R. Teague, T. Henning, S. Guilloteau, E. A. Bergin, D. Semenov, A. Dutrey, M. Flock, U. Gorti, T. Birnstiel, *Astro. J.* **864**, *133* (2018).

[13] S. M. Andrews, D. J. Wilner, A. M. Hughes, C. Qi, K. A. Rosenfeld, K. I. Öberg, T. Birnstiel, C. Espaillat, L. A. Cieza, J. P. Williams, S.-Y. Lin, P. T. P. Ho, *Astro. J.* **744**, *162* (2012).

[14] C. Favre, L. I. Cleeves, E. A. Bergin, C. Qi, G. A. Blake, *Astro. J. Lett.* **776**, *L38* (2013).

[15] R. Teague, S. Guilloteau, D. Semenov, Th. Henning, A. Dutrey, V. Piétu, T. Birnstiel, E. Chapillon, D. Hollenbach, U. Gorti, *A&A* **592**, *A49* (2016).

[16] E. Macías, O. Guerra-Alvarado, C. Carrasco-González, A. Ribas, C. C. Espaillat, J. Huang, S. M. Andrews, *A&A* **648**, *A33* (2021).

[17] J. K. Calahan, E. Bergin, K. Zhang, R. Teague, I. Cleeves, J. Bergner, G. A. Blake, P. Cazzoletti, V. Guzmán, M. R. Hogerheijde, J. Huang, M. Kama, R. Loomis, K. Öberg, C. Qi, E. F. van Dishoeck, J. T. van Scheltinga, C. Walsh, D. Wilner, *Astro. J.* **908**, *8* (2021).

[18] U. Gorti, D. Hollenbach, J. Najita, I. Pascucci, *Astro. J.* **735**, *90* (2011).

[19] M. Kama, S. Bruderer, E. F. van Dishoeck, M. Hogerheijde, C. P. Folsom, A. Miotello, D. Fedele, A. Belloche, R. Güsten, F. Wyrowski, *A&A* **592**, *A83* (2016).

[20] J. Huang, S. M. Andrews, L. I. Cleeves, K. I. Öberg, D. J. Wilner, X. Bai, T. Birnstie, J. Carpenter, A. M. Hughes, A. Isella, L. M. Pérez, L. Ricci, Z. Zhu, *Astro. J.* **852**, *122* (2018).

[21] T. Tsukagoshi, H. Nomura, T. Muto, R. Kawabe, D. Ishimoto, K. D. Kanagawa, S. Okuzumi, S. Ida, C. Walsh, T. J. Millar, *Astro. J. Lett.* **829**, *L35* (2016).

[22] J. D. Ilee, C. Walsh, J. Jennings, R. A. Booth, G. P. Rosotti, R. Teague, T. Tsukagoshi, H. Nomura, *MNRAS* **515**, *L12* (2022).

[23] D. Carrera, A. Johansen, M. B. Davies, *A&A* **579**, *A43* (2015).

[24] Y. Fukuharam S. Okuzumi, *Pub. Astron. Soc. Jap.* **76**, *708* (2024).

[25] N. I. Shakura, R. A. Sunyaev, *Astron. & Astrophys.* **24**, *337* (1973).

[26] J. E. Pringle, *Ann. Rev. Atron. Astrophys.* **19**, *137* (1981).

[27] N. A. Inogamov, R. A. Sunyaev, *Astron. Lett.* **36**, *848* (2010).

[28] Y. Nakagawa, M. Sekiya, C. Hayashi, *Icarus* **67**, *375* (1986).

[29] L. Puentes-Milián, *Rev. Cub. Fís.* **43**, *2* (2026).

[30] L. Puentes-Milián, E. García-Alfonso, M. Márquez-Mijares, J. Rubayo-Soneira, *Chem. Phys. Chem.* **e202300406** (2023).

[31] L. Puentes-Milián, E. García-Alfonso, M. Márquez-Mijares, J. Rubayo-Soneira, *Chem. Phys. Lett.* **849**, *141427* (2024).

[32] L. Puentes-Milián, A. Monteagudo-Rivero, *Int. J. Mod. Phys. D* **34**, *2550078* (2025).

[33] L. Puentes-Milián, *Petro. Chem. Indus. Intern.* **9**, *1* (2026).

[34] L. Puentes-Milián, *J. Astrophys. Astr.* **47**, *58* (2026).

[35] M. Márquez-Mijares, E. García-Alfonso, L. Puentes-Milián, J. Rubayo-Soneira, *An. Acad. Cienc. Cuba* **15**, *e3114* (2025).

[36] L. Puentes-Milián, *being reviewed by Astrophysics and Space Sciences* (2026).

[37] R. L. Burden, J. D. Faires, *Numerical Analysis*, Brooks/Cole Cengage Learning: Boston (2010).

[38] C. Iliadis, *Nuclear Physics of Stars*, WILEY-VCH Verlag GmbH & Co. KGaA (2007).

[39] K. S. Krane, *Introductory Nuclear Physics*, John Wiley & Sons (1988)

[40] R. J. Blin-Stoyle, *Eureka! Physics of Particles, Matter and the Universe*, Institute of Physics Publishing Bristol and Philadelphia (1997).

[41] R. Reifarth, P. Erbacher, S. Fiebiger, K. Göbel, T. Heftrich, M. Heil, F. Käppeler, N. Klapper, D. Kurtulgil, C. Langer, C. Lederer-Woods, A. Mengoni, B. Thomas, S. Schmidt, M. Weigand, M. Wiescher, *Eur. Phys. J. Plus* **133**, *424* (2018).